



Assembly of TiO₂ ultrathin nanosheets with surface lattice distortion for solar-light-driven photocatalytic hydrogen evolution



Shan Hu^a, Panzhe Qiao^a, Liping Zhang^b, Baojiang Jiang^{a,*}, Yanting Gao^a, Feng Hou^a, Baogang Wu^a, Qi Li^a, Yong Jiang^c, Chungui Tian^a, Wei Zhou^a, Guohui Tian^a, Honggang Fu^{a,*}

^a Key Laboratory of Functional Inorganic Material Chemistry, Ministry of Education of the People's Republic of China, Harbin Institute of Technology Shenzhen Graduate School, Shenzhen 518055, PR China

^b Department of Chemistry and Biochemistry, Kent State University, Kent, OH 44242, United States

^c Sun Yat-Sen University, PR China

ARTICLE INFO

Keywords:
TiO₂ ultrathin nanosheets
Assembly
Solar-light
Photocatalysis
Hydrogen evolution

ABSTRACT

Atomically two-dimensional semiconductor nanomaterials have drawn tremendous attention in photocatalytic applications due to their unique and remarkable properties. Herein, the assembly of TiO₂ ultrathin nanosheets was fabricated from the titanate sheets using a gas-assisted liquid exfoliation method combined with hydrogenation treatment strategy. The hydrogenation treatment can introduce more surface point defects such as oxygen vacancies without damaging the ultrathin two-dimensional structure. The ultrathin two-dimensional assembly has high percentages of low-coordinated surface atoms and large specific surface areas (340 m²/g), which could increase the absorption of photon and accelerate the photocatalytic reaction process. Meanwhile, homogeneous oxygen vacancies and large fraction of low-coordinated surface atoms in TiO₂ nanosheets can cause surface lattice distortion, which leads to a reduction in band gap and an upshift of conduction band minimum. The assembly possesses strong solar-light absorption, efficient charge transfer, and more surface-reactive sites for photocatalytic reactions. As a result, the assembly exhibits fast photocatalytic hydrogen evolution rate of 540.7 μmol h⁻¹ (30 mg catalyst) and good cycling stability under simulated solar irradiation. This work may provide perspectives for designing two-dimensional semiconductor materials besides TiO₂ ultrathin nanosheets as photocatalysts.

1. Introduction

At present, semiconductor photocatalysis is still considered as a promising technology to solve many energy and environment-related issues [1–4]. Among a large number of semiconductors some have been found capable of splitting water into hydrogen and oxygen by utilizing solar energy, providing a possibility to replace fossil fuels [5–8]. Titanium dioxide, TiO₂, is a popular semiconductor photocatalyst that has attracted considerable attention in the past several decades [9–11]. It has been used widely for photocatalytic hydrogen evolution, owing to its favorable chemical stability, nontoxicity, and high photocatalytic activity [12–14]. However, TiO₂ still faces some drawbacks such as wide band-gap and fast recombination of charge carriers, which limit its further application in solar-light-driven photocatalysis [15,16]. Hence, an important research aspect of TiO₂ for hydrogen energy application lies in the exploration of strategies to make it solar-light-responsive.

Ultrathin two-dimensional (2D) materials show great potential to

achieve high photocatalytic performance due to their unique morphology and physicochemical properties [17–19]. So far, many semiconductor materials with ultrathin 2D structures have been prepared and applied in photocatalysis, such as 2D TiO₂, ZnO, WO₃, Fe₂O₃, and so on [20–22]. As compared to their bulk structures, ultrathin 2D semiconductors have larger specific surface areas and higher percentages of low-coordinated surface atoms, which are beneficial to the photon absorption. Besides, the migration of electron-hole pairs are likely to be improved due to the atomic-scale thickness of the 2D materials [23–25]. Further, 2D structures with high amounts of surface atoms are able to provide more reactive sites, leading to faster photocatalytic reactions under light irradiation. It's noteworthy that surface atoms in ultrathin 2D materials have large chances to escape from the lattices to form point defects, such as oxygen vacancies, which may cause the distortion of surface lattices, resulting in narrower band-gaps and higher catalytic activity [26–28].

The typical strategies for the preparation of 2D semiconductor materials are the bottom-up and the top-down approaches [29,30]. The

* Corresponding authors.

E-mail addresses: jiangbaojiang88@sina.com (B. Jiang), fuhg@vip.sina.com, fuhg@hlju.edu.cn (H. Fu).

former includes self-assembly and oriented attachment strategy [31], while the latter includes liquid exfoliation, which can be used for layered semiconductor materials with weak interlayer van der Waals forces [32]. Although both the bottom-up and the top-down methods have been extensively investigated, a combination strategy, for instance, liquid exfoliation combined with hydrogenation treatment, which may bring unexpected advantages, is rarely studied to get 2D materials [33]. In addition, the assembly of 2D sheets could inhibit their aggregation, ensuring the effective exposure of reaction sites. During the cycling photocatalysis process, the collection of assembly is also easy and effective.

Herein, we developed a simple approach to fabricate an assembly of TiO_2 ultrathin nanosheets. During the synthetic procedure, a gas assisted liquid exfoliation technology was used to prepare the precursor, titanate hydroxide ultrathin sheets, which were converted into ultrathin TiO_2 nanosheets after hydrogenation treatment, resulting in the TiO_2 ultrathin nanosheet assembly. This assembly possesses a narrow bandgap, large specific surface area, and efficient charge transfer. As a consequence, it exhibited excellent photocatalytic performance for hydrogen evolution under AM 1.5 light irradiation. Morphology and electronic structural characterizations were carried out to investigate the influence of 2D assembly structure on the photocatalytic performance, and a possible photocatalytic mechanism was also discussed.

2. Experimental

2.1. Materials

Titanyl sulfate (93%) and commercial anatase TiO_2 were purchased from Sigma-Aldrich Trading Co. Ltd. Ammonium hydroxide (25%) was purchased from Tianjin Kermel limited company. All chemical reagents were obtained from commercial reagents company without further purification. The deionized water was used in the experimental process.

2.2. Preparation of TiO_2 assembly

Firstly, 10 mL of ammonium hydroxide was quickly mixed with 0.06 g of titanyl sulfate, and then to the mixture 30 mL of deionized water was added. After stirring vigorously for 12 h to form a homogeneous solution, the resultant suspension was transferred to a 50-mL Teflon-lined autoclave and heated to 160 °C for 6 h. Next, the precipitate was collected, washed successively using deionized water and ethanol several times, and dried in a vacuum oven at 60 °C for 8 h to obtain the white powers. Subsequently, the as-prepared white powders were calcinated in H_2 flow (hydrogen purity: ≥ 99.999%, gas velocity: 80 mL min⁻¹) at 300 ~ 600 °C for 2 h under normal pressure conditions, with a constant heating rate of 10 °C min⁻¹, the calcination products were denoted as H₂-T, where T = 300, 400, 500, and 600. Additionally, a reference sample named as Air-500 was obtained by calcining the white powders in air at 500 °C for 3 h (heating rate: 1 °C min⁻¹). Many other reference samples and related experimental conditions are shown in the supporting information.

2.3. Characterization

The crystalline structures were obtained by X-ray powder diffraction (XRD, Rigaku D/max-IIIB with Cu K α , λ = 1.5406 Å radiation) at an accelerating voltage of 40 kV and emission current of 40 mA. Morphologies of the samples were investigated by using a Hitachi S-4800 field emission scanning electron microscope (SEM) operating at 15 KV and a JEOL model JEM 2100 EX transmission electron microscope (TEM) with an acceleration voltage of 200 kV. Raman measurements were performed with a Jobin Yvon HR800 micro-Raman spectrometer at 457.9 nm. Photoluminescence (PL) spectra of the photocatalysts were recorded on a Hitachi F-4600 fluorescence spectrophotometer. The Brunauer-Emmett-Teller (BET) surface area was

determined in the range of relative pressure (p/p_0) from 0 to 0.2 by using a Tristar II 3020 surface area and porosity analyzer (Micromeritics). Pore size distribution curves were obtained using the Barrett-Joyner-Halenda (BJH) method from the adsorption data. UV-vis diffuse reflectance spectra were determined by a UV-vis spectrophotometer (Shimadzu UV-2550). The X-ray photoelectron spectroscopy (XPS, VG ESCALAB MK II) measurements were performed on a system with a monochromatized Mg K α line source (1253.6 eV). All binding energies were calibrated by referencing to the C 1 s peak at 284.6 eV. The electron spin resonance (ESR) spectra were collected by using a Bruker ER200DSRC10/12 spectrometer at 9.4 GHz at 300 K with 1 mW, magnetic field: 0–2 T. The surface photovoltage (SPS) measurements of the samples were carried out in a home-built apparatus. Scanning Kelvin Probe (SKP) measurements (SKP5050 system, Scotland) were conducted under normal laboratory conditions (in ambient atmosphere). The electrochemical impedance spectroscopy (EIS) was analyzed by an electrochemical workstation (Princeton Versa STAT). Sample films on FTO (Fluorine doped SnO_2 layer, 20 Ω per square, Nippon sheet glass, Japan) prepared by pyrolysis was used as the working electrode; Pt foil and Ag/AgCl were employed as the counter electrode and the reference electrode, respectively; the electrolyte was 0.1 M KOH. Luminescence lifetimes were determined by an Edinburgh FLS 920 fluorescence spectrophotometer.

Photocurrent measurements were performed by using a three-electrode configuration, with the abovementioned sample films as the working electrodes, saturated Ag/AgCl as the reference electrode, and platinum foil (3 × 2 cm) as the counter electrode. 1 M KOH (pH = 13.6) purged with N_2 was used as the electrolyte. The working electrode films (1.0 × 1.0 cm²) were prepared by doctor-blade method, in which sample paste was introduced onto FTO by using a thin glass rod. All working electrodes were subsequently dried in an oven and calcined at 350 °C for 90 min under a flow of nitrogen (heating rate: 2.5 °C min⁻¹). 1 M KOH aqueous solution was used as the electrolyte. The transient photocurrent responses were investigated by several on-off cycles simulated sunlight irradiation (AM 1.5).

2.4. Photocatalytic hydrogen evolution measurement

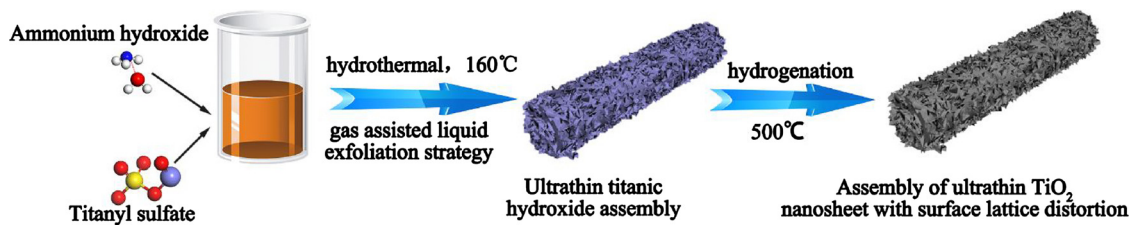
The photocatalytic hydrogen evolution experiment was conducted in an online photocatalytic hydrogen production system (AuLight, Beijing, CELSPH₂N), connected to an online gas chromatograph (SP7800, TCD, molecular sieve 5 Å, Beijing Keruida Limited) using nitrogen as the carrier gas at 20 °C. Firstly, a suspension was prepared by mixing 30 mg of the catalyst with 80 mL of distilled water and 20 mL of methanol in the reaction cell under stirring. Pt (1 wt %), which came from H_2PtCl_6 , was loaded onto the photocatalysts in aqueous solution. Prior to the reaction, the mixture was deaerated by evacuation to remove O_2 and CO_2 dissolved in water. An AM 1.5 solar power system (solar simulator, Oriel, USA) equipped with an AM 1.5 G filter (Oriel, USA) was used as the light source. The gas evolved was collected and analyzed at a 1-h interval.

The determination of the apparent quantum efficiency (AQE) for hydrogen generation was performed using the same closed circulating system under illumination of a 300 W Xe lamp with different bandpass filters (313, 365, 420, 450 and 520 nm). AQE at different wavelengths was calculated by using the following equation:

$$\text{AQE} = \frac{2 \times \text{number of } \text{H}_2 \text{ molecules evolved}}{\text{number of incident photons}} \times 100\%$$

3. Results and discussions

In general, titanium source in an alkaline solution is used as the precursor to synthesize layered protonated titanate nanosheets [34]. Herein, titanyl sulfate was selected as the starting compound for the formation of ultrathin titanate sheets, which were converted



Scheme 1. Illustration of synthesis of the TiO_2 ultrathin nanosheets assembly.

into TiO_2 nanosheets assembly eventually. The possible growth mechanism is illustrated in Scheme 1. During the experimental process, ammonium hydroxide was quickly added into the titanyl sulfate solution, followed by hydrothermal reaction, resulting in ultrathin titanic hydroxide precursor based on the self-assembly of titanic hydroxide molecules (Figure S1). The titanic hydroxide is the main component of precursor. The surface morphology change of the titanic hydroxide precursor through the hydrothermal process was monitored (Figure S2). In the beginning of the hydrothermal reaction (10 min), the resultant solid showed smooth surface. As reaction time was increased, many small flakes started to emerge on the surface. Adequate reaction time such as six hours is beneficial to the formation of ultrathin titanic hydroxide sheet assembly. Titanic hydroxide nanosheets with atomic thickness can be prepared by using a gas-assisted liquid exfoliation method. Ammonia gas molecules produced during the hydrothermal reaction were able to overcome the Van der Waals forces between titanic hydroxide layers, resulting in ultrathin nanosheets. Therefore, hydrothermal treatment and ammonia exfoliation are two crucial factors toward the fabrication of ultrathin 2D titanic hydroxide (Figure S3 and S4). Eventually, the obtained precursor were transformed into an assembly of TiO_2 ultrathin nanosheets by thermal treatment under hydrogen. The advantage of these ultrathin laminar structures with defects and their catalytic performances will be described in detailed.

The morphology and the internal structure of TiO_2 ultrathin nanosheet assembly were characterized by TEM and SEM and shown in Fig. 1, Figure S5 and S6. As can be seen, the typical sample H₂-500 from hydrogenation treatment appears to be a one-dimensional assembly structure (Figure S5), which is formed by nanosheets with random

orientations. TEM images further confirm that the internal structure of 2D nanosheets. The overall 2D nanosheets were well preserved with some shrinkage in size, and the thickness of nanosheets is in the range 0.613 ~ 0.937 nm based on the analysis of many TEM images (Fig. 1a-d and Figure S6). Moreover, it shows large specific surface area ($340 \text{ m}^2/\text{g}$). While the sample obtained by calcination in air only shows irregular structures (Figure S7). The hydrothermal sample calcined under hydrogen will form disordered structure and surface oxygen vacancy, so the ultrathin nanosheets structure will not be damaged obviously. However, the hydrothermal sample calcined in the air is a process of rapid crystallization. Without the protection of disordered structure, the crystal is complete and the particle structure is formed. Therefore, the hydrogenation treatment is not only able to keep the structure of the ultrathin nanosheets but introduce surface point defects to modify their electronic structure.

The HRTEM images further reveal the crystal structure details of H₂-500. Fig. 1c, d exhibit clear lattice fringes with spacings of 0.348 nm and 0.346 nm, which are close to the (101) spacing (0.35 nm) of TiO_2 anatase phase, suggesting that TiO_2 sheets grow along [010] and [100] direction [35,36]. It is interesting that the lattice fringes of H₂-500 are narrower than that of the standard (101) interplanar spacing of anatase TiO_2 . The lattice distortion may be ascribed to low-coordinated surface atoms and surface point defects in ultrathin TiO_2 , such as oxygen vacancies (OV).

The crystal structures of H₂-500 and reference samples were investigated by X-ray diffraction (XRD) (Fig. 1e). It can be seen in Fig. 1e, the as-produced Air-500 and commercial reference samples all show anatase phase of TiO_2 (JCPDS No. 21-1272). Well-defined diffraction

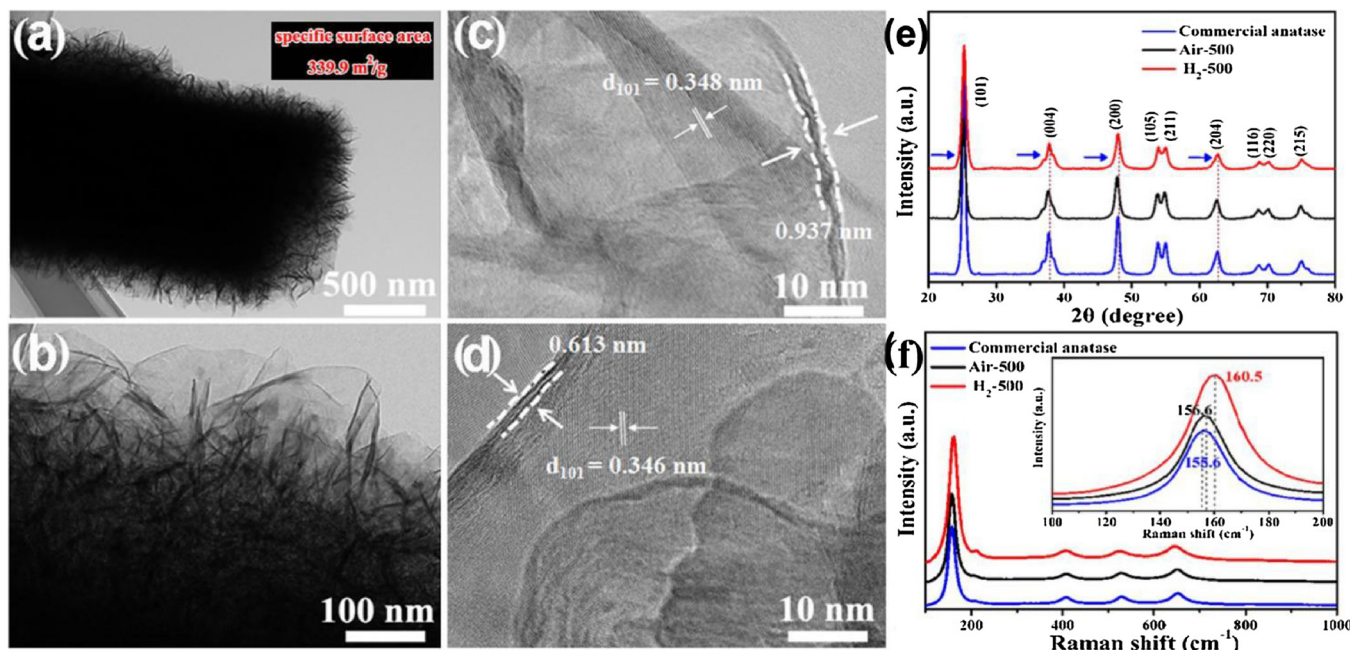


Fig. 1. TEM images (a), (b) and HRTEM images (c), (d) of typical H₂-500 sample, respectively. H₂-500 shows large specific surface area ($340 \text{ m}^2/\text{g}$). XRD patterns (e) of H₂-500 and reference samples; Raman spectra (f) of Air-500 and H₂-500.

peaks at 25.28, 37.82, 47.97, 53.96, 54.94 and 62.57° can be indexed as (101), (004), (200), (105), (211) and (204) planes of nanocrystalline anatase TiO_2 [37]. However, as compared with the abovementioned data, XRD pattern of the sample $\text{H}_2\text{-}500$ reveals different diffraction angles (2θ) at 25.34, 37.98, 48.01, 54.06, 55.05, and 62.78°. The shift of diffraction angles of $\text{H}_2\text{-}500$ toward higher values implies the decrease in crystal interplanar distance, which is consistent with the HRTEM results. The change of crystalline structure can be attributed to low-coordinated surface atoms and presence of oxygen vacancies in ultrathin 2D structure.

The structural changes were further studied by Raman spectroscopy (Fig. 1f). Five peaks at 156.6, 210, 408, 526, and 644 cm^{-1} of Air-500 can be ascribed to the typical anatase TiO_2 Raman bands of E_g , E_g , B_{1g} , A_{1g} (B_{1g}), and E_g modes, respectively [38]. As compared with Air-500 and commercial anatase, the in-plane softening mode E_g of $\text{H}_2\text{-}500$ exhibits a clear red shift from 156.6 cm^{-1} to 160.5 cm^{-1} , and all peaks also show band broadening. In general, Raman mode softening causes shift of bands towards lower wavenumbers for ultrathin materials, which could be ascribed to the phonon confinement effect. Further, the surface O-vacancies in ultrathin 2D TiO_2 due to hydrogen treatment could also give rise to the red shift. In this work, the Raman shift is mainly attributed to the effect of surface O-vacancies.

It has been reported that single-electron-trapped vacancy-type defects in semiconductor materials can be identified by electron spin resonance (ESR) [39,40]. Fig. 2a shows the ESR pattern of the typical sample $\text{H}_2\text{-}500$, which is different from that of Air-500 in Figure S8. An obvious and symmetrical ESR signal for $\text{H}_2\text{-}500$ can be observed at $g \approx 1.999$ (Fig. 2a), which is considered to be an indication of electrons being captured by OVs [41]. Therefore, thermal treatment under hydrogen gas is capable of producing plenty of OVs without damaging the 2D structure. Furthermore, the atomic-scale thickness, large surface area, and high fraction of coordinatively unsaturated surface atoms of

TiO_2 ultrathin sheets will provide them with superior electronic properties and adequate surface-active sites, which may lead to the improvement of photocatalytic activity.

The chemical state of the surface oxygen for the $\text{H}_2\text{-}500$ sample can be determined by X-ray photoelectron spectroscopy (XPS) measurements. As shown in Fig. 2b, the main peak at 529.3 eV can be assigned to the lattice oxygen of TiO_2 , and the signal at a higher binding energy of 530.7 eV can be ascribed to the formation of oxygen vacancies on the surface [42]. Figure S9 displays the high-resolution XPS spectrum of Ti 2p of $\text{H}_2\text{-}500$, which shows two peaks located at 458.1 and 464.0 eV, corresponding to the split signals of Ti^{4+} in $\text{H}_2\text{-}500$ [43]. The formation of Ti^{3+} species in the $\text{H}_2\text{-}500$ was also confirmed by the appearance of signals at 457.4 and 462.9 eV [44]. The Ti^{3+} species were created as a result of the Ti^{4+} reduction during the hydrogenation treatment at high temperature. The XPS survey spectrum of $\text{H}_2\text{-}500$ is shown in Figure S10. According to the peaks of O 1s and Ti 2p, the existence of Ti^{3+} defects and oxygen vacancies in $\text{H}_2\text{-}500$ can be further verified. Ti^{3+} defects and oxygen vacancies are expected to change the band structure of the material, promoting the separation of photoinduced electrons and holes during the photocatalytic process.

Nitrogen adsorption-desorption isotherms and pore size distributions curves of Air-500 and $\text{H}_2\text{-}500$ samples are shown in Fig. 2c. It can be seen that $\text{H}_2\text{-}500$ has the type IV isotherms, indicating the existence of mesopores [45]. Furthermore, the hysteresis loop of the sample belongs to the type H3 according to the International Union of Pure and Applied Chemistry (IUPAC) classification, which suggests that these layered materials have slit-like pores arising from the assembly of TiO_2 nanosheets [46]. The isotherms show large amount of nitrogen adsorbed at high P/P_0 (approaching to 1.0), implying the formation of large mesopores. This result is in good agreement with the TEM observations, which reveal TiO_2 nanosheets and their assembly as shown in Fig. 1. Thermal treatments in air and H_2 (i.e., hydrogenation) can be

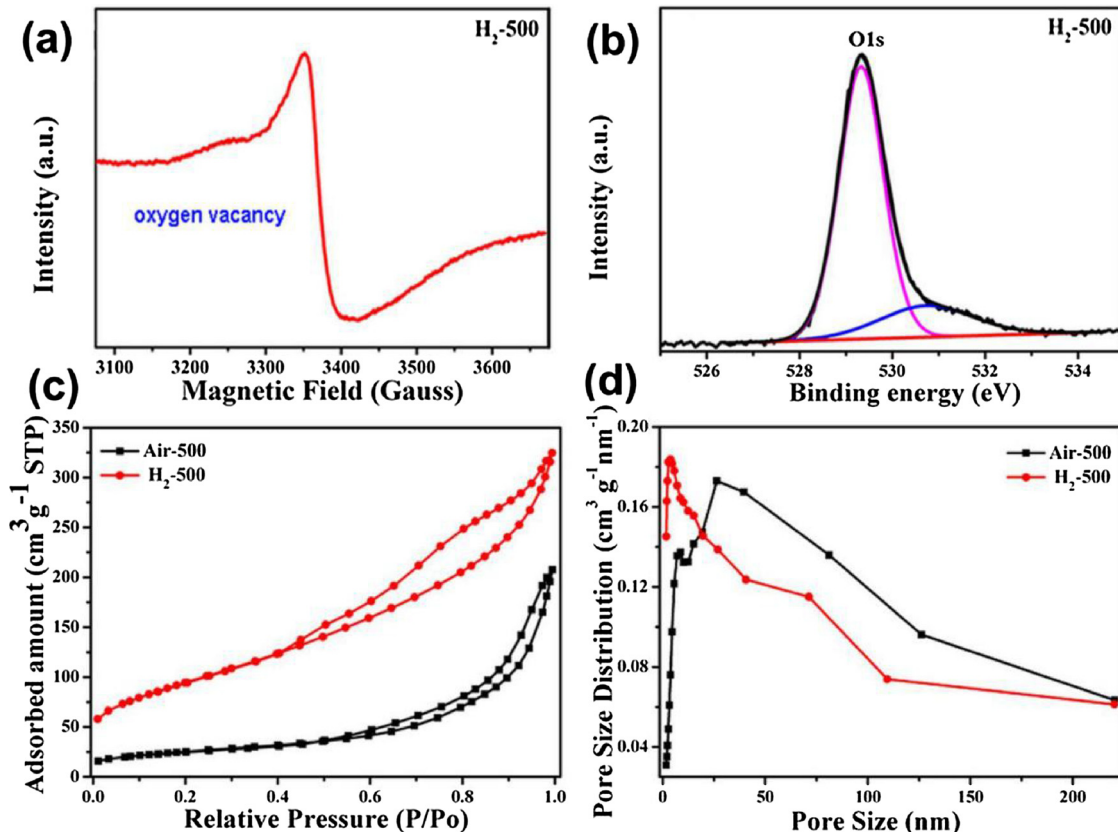


Fig. 2. The ESR spectrum (a) and XPS O1s patterns (b) of $\text{H}_2\text{-}500$. N_2 adsorption-desorption isotherms (c) and BJH pore-size distribution curves (d) of Air-500 and $\text{H}_2\text{-}500$.

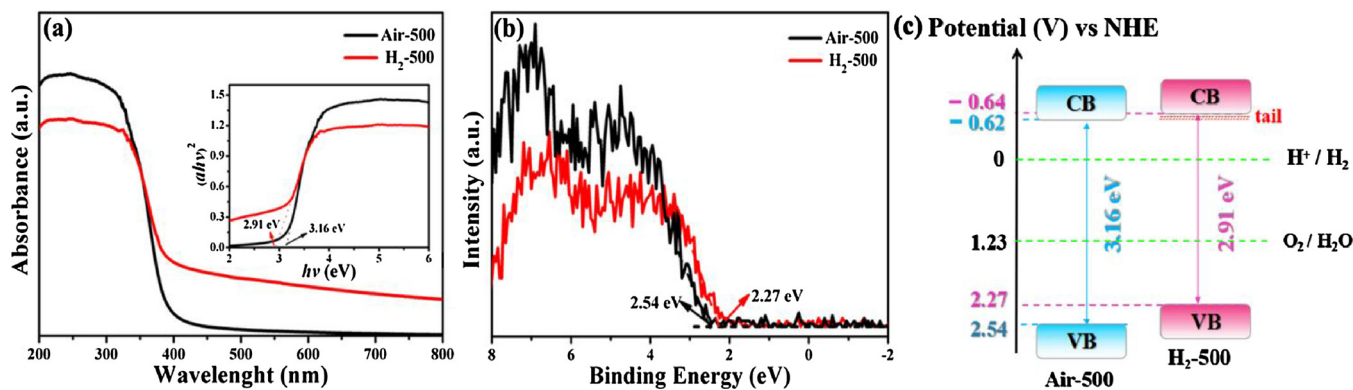


Fig. 3. UV-vis reflectance spectra (a), inset is the corresponding Tauc plots of Air-500 and H₂-500, respectively, for the determination of optical band-gaps; XPS valence band spectra (b) of Air-500 and H₂-500; Energy band diagrams (c) of Air-500 and H₂-500.

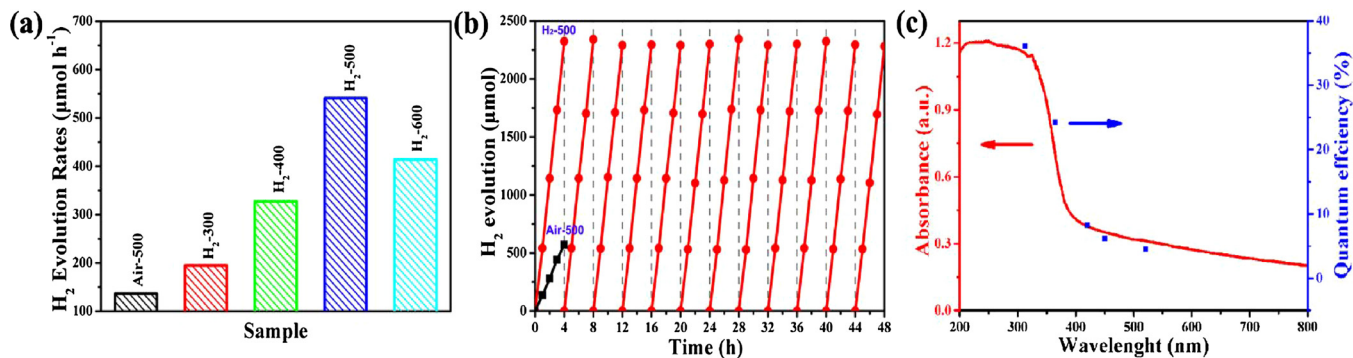


Fig. 4. (a) Photocatalytic H₂ evolution rate for different catalysts using AM 1.5 illumination; (b) The recycled photocatalytic measurement of H₂-500 for H₂ evolution, each of the experiment lasted 4 h, and then the catalyst was recycled and used for the next 4 h cycle. (c) Wavelength-dependent apparent quantum efficiency (AQE) for H₂ evolution over H₂-500 (right axis) and UV-vis light absorption spectrum of H₂-500 (left axis).

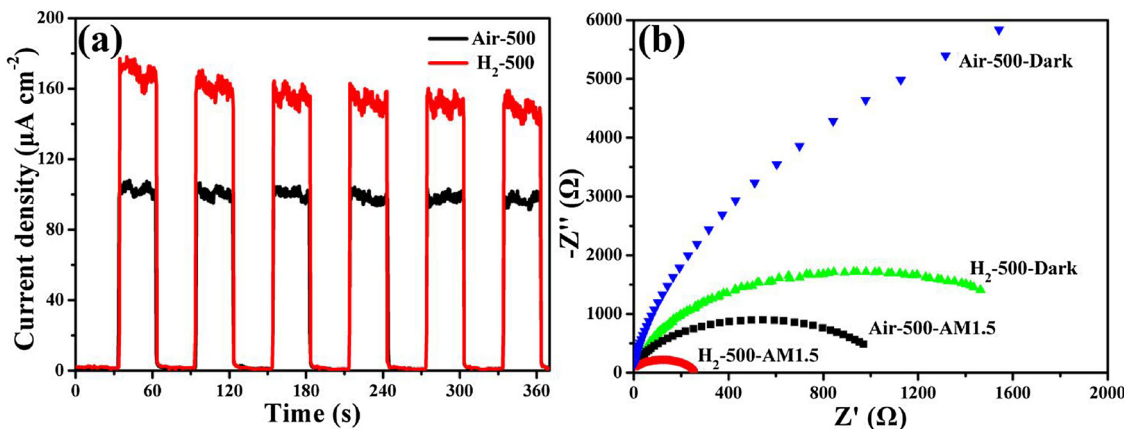


Fig. 5. (a) Transient photoelectrochemical responses for Air-500 and H₂-500 under AM1.5 illumination and (b) electrochemical impedance spectroscopy of Air-500 and H₂-500 under dark and AM1.5 illumination.

seen to result in quite different porosity. The BET surface area, pore size and pore volume for Air-500 and H₂-500 were calculated to be $91 \text{ m}^2 \text{ g}^{-1}$, 12.4 nm, $0.28 \text{ cm}^3 \text{ g}^{-1}$, and $340 \text{ m}^2 \text{ g}^{-1}$, 5.5 nm, $0.47 \text{ cm}^3 \text{ g}^{-1}$, respectively. For sample H₂-500, the hydrothermal sample calcined under hydrogen will form disordered protective layer structure and surface oxygen vacancy, so the ultrathin nanosheets structure will not be damaged obviously. Meanwhile, the ultrathin nanosheets structure will exhibit high BET. However, the calcination of hydrothermal sample in air is a process of rapid crystallization. Without the protection of disordered structure, the crystal is large particle structure. Therefore, the bulk Air-500 only has low BET data. Due to their high specific surface areas, the samples can provide a large number of

reaction sites, favoring catalytic reactions.

Since the photocatalytic performance of a material is greatly dependent on its optical absorption property; therefore, UV-vis absorption spectra of the samples were recorded (Fig. 3a). For Air-500, its absorption spectrum is similar to that of anatase TiO₂ reported [47,48]. Nevertheless, after hydrogenation, the absorption edge was extended from the UV light region to the visible light region, which is in agreement with the color change from white to grey (Fig. 3a). The increased light absorption strength can be ascribed to the multiple scattering in the pore structure and large absorption surface of the nanosheets. Simultaneously, the number of available photons and electrons generated is risen, which can enhance long-wavelength light utilization. Fig. 3b

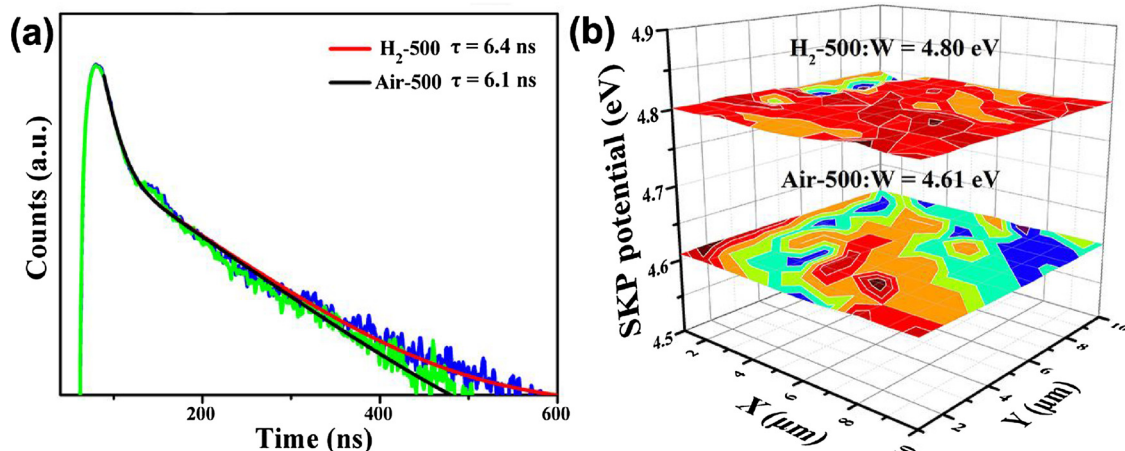


Fig. 6. Transient fluorescence spectrum (a) and scanning Kelvin probe maps (b) of Air-500 and H₂-500.

shows XPS valence band (VB) spectra of H₂-500 and Air-500. The CB minimum for Air-500 is located at -0.62 eV, while that of the H₂-500 is at -0.64 eV, corresponding to a 0.02 eV upward shift of the CB edge in H₂-500. On the other hand, hydrogenation introduces surface oxygen vacancies, generating defect states in the band gap. As a result, the band gap was decreased from 3.16 eV for Air-500 to 2.91 eV for H₂-500 (Fig. 3a), which improves visible light harvesting efficiency. The band structure variations not only help the H₂-500 harvest more solar light, but also accelerate electron transfer, thus achieving higher photocatalytic activity. In fact, the upshift of conduction band position would significantly improve protons' reduction power of photocatalyst, resulting in promoted photocatalytic activity. The energy band diagrams of Air-500 and H₂-500 are shown in Fig. 3c.

The photocatalytic hydrogen production performance of Air-500, H₂-300, H₂-400, H₂-500 and H₂-600 was evaluated under simulated sunlight irradiation (AM 1.5). As shown in Fig. 4a, H₂-500 displays the highest photocatalytic H₂ evolution rate of 540.7 $\mu\text{mol h}^{-1}$ (30 mg catalyst) and apparent quantum efficiency of 8.29% at 420 nm (Fig. 4c), which is higher than Air-500, demonstrating that TiO₂ nanosheets can effectively increase visible-light harvesting and promote the separation and transfer of photo-induced electrons and holes. The photocatalytic performance was also found to be higher than previous reports (Table S1). Moreover, recyclability test of H₂-500 also confirmed its high stability during photocatalytic hydrogen production (Fig. 4b). After 12 cycles of 4-hour experiment, H₂-500 still showed high catalytic activity.

Benefiting from the unique atomic structure and surface defects, ultrathin 2D assembly materials can achieve enhanced solar light harvesting, possibly promoting its electrochemical properties. The transient photocurrent responses were measured (Fig. 5a). Clearly, H₂-500 shows much stronger photocurrent responses than Air-500 owing to easy and quick electron transport within the 2D structure; as a result, more efficient separation and transfer of charge carriers would be gained. Meanwhile, the photocurrent responses do not decay distinctly with increase of illuminated time, implying good photoelectrochemical stability of sample H₂-500. Fig. 5b exhibits Nyquist impedance spectra for H₂-500 and Air-500 under dark and AM 1.5. According to electrochemical impedance mechanism, the electrochemical impedance spectroscopy shows smaller interfacial resistance for H₂-500 electrode under dark and AM 1.5 than that of Air-500 electrode at the same conditions, indicating that the H₂-500 electrode has better conductivity. Moreover, the Nyquist plots for the H₂-500 catalyst are consistent with the tendency of the photocurrent responses results, which suggests that the TiO₂ ultrathin nanosheet assembly possesses enhanced electronic transfer properties as compared to zero-dimensional TiO₂ nanoparticles.

In order to study the mechanism of the enhancement in

photocatalytic property, surface photovoltage spectroscopy (SPS) was performed, which is a well-established noncontact technique to investigate the charge dynamics of semiconductors, such as the separation and transport of electrons and holes. The surface photovoltaic spectral response maxima of H₂-500 and Air-500 are observed at 350 nm and 336 nm, respectively (Figure S11), suggesting that H₂-500 has a higher carrier separation efficiency. Steady-state photoluminescence (PL) spectroscopy was conducted to evaluate the separation and the transport of photogenerated electrons and holes (Figure S12). It can be seen that the fluorescence intensity of H₂-500 is lower than that of Air-500 in the UV region, implying a less degree of charge annihilation in H₂-500 compared to Air-500. Both the SPS and PL results clearly support that H₂-500 is superior to Air-500 in photocatalytic hydrogen production.

The lifetimes of photogenerated electron-hole pairs in H₂-500 and Air-500 were also analyzed by transient fluorescence spectra (Fig. 6a). The results show that fluorescence lifetime of H₂-500 is 6.4 ns, which is longer than that of Air-500 (6.1 ns). The surface work functions (ϕ) of Air-500 and H₂-500 were found to be 4.61 and 4.80 eV, respectively (Fig. 6b). The higher work function indicates that the approximate Fermi level of H₂-500 is lower than that of Air-500, which affects the built-in electronic field and the surface band bending. Simultaneously, the lower Fermi level could accelerate the photogenerated electron transfer to the surface, thus greatly reducing the electron-hole recombination. Therefore, the enhanced performance is mainly attributed to the following factors: (I) large number of surface reaction sites on the ultrathin TiO₂ nanosheets; (II) lattice distortion effect due to surface point defects (oxygen vacancies) which changes the energy band structure, resulting in stronger absorption of visible light and more efficient separation and transport of charge carriers.

4. Conclusion

In summary, we have demonstrated an effective gas-assisted liquid exfoliation method combined with hydrogenation treatment to prepare ultrathin TiO₂ nanosheet assembly. The close correlation between defects, electronic structure, and catalytic properties has also been investigated. The ultrathin 2D structure and surface OVs are able to bring about surface lattice distortion. Meanwhile, ultrathin structures prompt the charge transfer, alleviating the recombination of photoinduced electron-hole pairs. As a result, ultrathin TiO₂ nanosheet assembly shows efficient solar-light utilization, narrow band-gap and significant amount of surface reactive sites. Consequently, the sample H₂-500 exhibited a fast solar-light-driven photocatalytic hydrogen evolution rate of 540.7 $\mu\text{mol h}^{-1}$ and high apparent quantum efficiency of 8.29% at 420 nm. This work regarding the TiO₂ ultrathin nanosheet assembly

structure may be helpful for the exploration of more novel semiconductor functional materials.

Notes

The authors declare no competing financial interest.

Acknowledgements

We gratefully acknowledge the support of this research by the National Natural Science Foundation of China (21631004, 21771061, 21571054, 51772079). Outstanding academic leaders of Harbin city (2016RAXXJ002).

Appendix A. Supplementary data

Supplementary material related to this article can be found, in the online version, at doi:<https://doi.org/10.1016/j.apcatb.2018.08.017>.

References

- [1] X.Q. Liu, J. locozzia, Y. Wang, X. Cui, Y.H. Chen, S.Q. Zhao, Z. Li, Z.Q. Lin, Energy Environ. Sci. 10 (2017) 402–434.
- [2] N.S. Lewis, Science 351 (2016) 353.
- [3] S.Y. Reece, J.A. Hamel, K. Sung, T.D. Jarvi, A.J. Esswein, J.J. Pijpers, D.G. Nocera, Science 334 (2011) 645–648.
- [4] Y. Ma, X.L. Wang, Y.S. Jia, X.B. Chen, H.X. Han, C. Li, Chem. Rev. 114 (2014) 9987–10043.
- [5] J. Liu, Y. Liu, N.Y. Liu, Y.Z. Han, X. Zhang, H. Huang, Y. Lifshitz, S.T. Lee, J. Zhong, Z.H. Kang, Science 347 (2015) 970–974.
- [6] Y.F. Zhao, X.D. Jia, G.I. Waterhouse, L.Z. Wu, C.H. Tung, D. O'Hare, T.R. Zhang, Adv. Energy Mater. 6 (2016) 1501974.
- [7] G.J. Liu, S. Ye, P.L. Yan, F.Q. Xiong, P. Fu, Z.L. Wang, Z. Chen, J.Y. Shi, C. Li, Energy Environ. Sci. 9 (2016) 1327–1334.
- [8] Q. Wang, T. Hisatomi, Q.X. Jia, H. Tokudome, M. Zhong, C.Z. Wang, Z.H. Pan, T. Takata, M. Nakabayashi, N. Shibata, Y.B. Li, I.D. Sharp, A. Kudo, T. Yamada, K. Domen, Nat. Mater. 15 (2016) 611–615.
- [9] X.Y. Liu, G.L. Zhu, X. Wang, X.T. Yuan, T.Q. Lin, F.Q. Huang, Adv. Energy Mater. 6 (2016) 1600452.
- [10] X.B. Chen, L. Liu, F.Q. Huang, Chem. Soc. Rev. 44 (2015) 1861–1885.
- [11] W. Zhou, F. Sun, K. Pan, G. Tian, B. Jiang, Z. Ren, C. Tian, H. Fu, Adv. Funct. Mater. 21 (2011) 1922–1930.
- [12] C.L. Chen, Y.L. Wei, G.Z. Yuan, Q.L. Liu, R.R. Lu, X. Huang, Y. Cao, P.H. Zhu, Adv. Funct. Mater. 27 (2017) 1701575.
- [13] W. Zhou, W. Li, J.Q. Wang, Y. Qu, Y. Yang, Y. Xie, K.F. Zhang, L. Wang, H.G. Fu, D.Y. Zhao, J. Am. Chem. Soc. 136 (2014) 9280–9283.
- [14] M. Li, Y. Chen, W. Li, X. Li, H. Tian, X. Wei, Z.H. Ren, G.R. Han, Small 13 (2017) 1604115.
- [15] Y. Ben-Shahar, F. Scognella, I. Kriege, L. Moretti, G. Cerullo, E. Rabani, U. Banin, Nat. Commun. 7 (2016) 10413–10420.
- [16] Y. Nakibli, Y. Mazal, Y. Dubi, M. Wachtler, L. Amirav, Nano Lett. 18 (2018) 357–364.
- [17] X.G. Meng, L.Q. Liu, S.X. Ouyang, H. Xu, D.F. Wang, N.Q. Zhao, J.H. Ye, Adv. Mater. 28 (2016) 6781–6803.
- [18] J.Z. Shang, C.X. Cong, Z.L. Wang, N. Peimyoo, L.S. Wu, C.J. Zou, Y. Chen, X.Y. Chin, J.P. Wang, C. Soci, W. Huang, T. Yu, Nat. Commun. 8 (2017) 543.
- [19] J. Di, J. Xiong, H.M. Li, Z. Liu, Adv. Mater. 30 (2018) 1704548.
- [20] W. Li, F. Wang, Y.P. Liu, J.X. Wang, J.P. Yang, L.J. Zhang, A.A. Elzatahry, D. Al-Dahyan, Y.Y. Xia, D.Y. Zhao, Nano Lett. 15 (2015) 2186–2193.
- [21] W. Li, J. Liu, D.Y. Zhao, Nat. Rev. Mater. 1 (2016) 16023.
- [22] B. Luo, G. Liu, L.Z. Wang, Nanoscale 8 (2016) 6904–6920.
- [23] Y.F. Sun, S. Gao, F.C. Lei, Y. Xie, Chem. Soc. Rev. 44 (2015) 623–636.
- [24] S. Gao, X.C. Jiao, Z.T. Sun, W.H. Zhang, Y.F. Sun, C.M. Wang, Q.T. Hu, X.L. Zu, F. Yang, S.Y. Yang, L. Liang, J. Wu, Y. Xie, Angew. Chem. Int. Ed. 55 (2016) 698–702.
- [25] J. Di, J.X. Xia, H.M. Li, Z. Liu, Nano Energy 35 (2017) 79–91.
- [26] J.W. Wan, W.X. Chen, C.Y. Jia, L.R. Zheng, J.C. Dong, X.S. Zheng, Y. Wang, W.S. Yan, C. Chen, Q. Peng, D.S. Wang, Y.D. Li, Adv. Mater. 30 (2018) 1705369.
- [27] B.J. Jiang, Y.Q. Tang, Y. Qu, J.Q. Wang, Y. Xie, C.G. Tian, W.Z.H.G. Fu, Nanoscale 7 (2015) 5035–5045.
- [28] Y. Jiang, H.Y. Ning, C.G. Tian, B.J. Jiang, Q. Li, H.J. Yan, X.L. Zhang, J.Q. Wang, L.Q. Jing, H.G. Fu, Appl. Catal. B: Environ. 229 (2018) 1–7.
- [29] H.T. Wang, H.T. Yuan, S.S. Hong, Y.B. Li, Y. Cui, Chem. Soc. Rev. 44 (2015) 2664–2680.
- [30] M. Nasilowski, B. Mahler, E. Lhuillier, S. Ithurria, B. Dubertret, Chem. Rev. 116 (2016) 10934–10982.
- [31] C.L. Tan, H. Zhang, Nat. Commun. 6 (2015) 7873–7885.
- [32] C.L. Tan, X.H. Cao, X.J. Wu, Q.Y. He, J. Yang, X. Zhang, J. Chen, W. Zhao, S.K. Han, G.H. Nam, M. Sindoro, H. Zhang, Chem. Rev. 117 (2017) 6225–6331.
- [33] Y.Q. Guo, K. Xu, C.Z. Wu, J.Y. Zhao, Y. Xie, Chem. Soc. Rev. 44 (2015) 637–646.
- [34] Y.J. Song, H. Wang, X.M. Gao, Y.X. Feng, S.J. Liang, J.H. Bi, S. Lin, X.Z. Fu, L. Wu, ACS Catal. 7 (2017) 8664–8674.
- [35] S. Selcuk, A. Selloni, Nat. Mater. 15 (2016) 1107–1112.
- [36] R.G. Li, Y.X. Weng, X. Zhou, X.L. Wang, Y. Mi, R.F. Chong, H.X. Han, C. Li, Energy Environ. Sci. 8 (2015) 2377–2382.
- [37] X.C. Zhang, W.Y. Hu, K.F. Zhang, J.Q. Wang, B.J. Sun, H.Z. Li, P.Z. Qiao, L. Wang, W. Zhou, ACS Sustain. Chem. Eng. 5 (2017) 6894–6901.
- [38] S. Piovesana, A.L. Capriotti, C. Cavaliere, F. Ferraris, D. Iglesias, S. Marchesan, A. Lagana, Anal. Chem. 88 (2016) 12043–12050.
- [39] Y. Nosaka, A.Y. Nosaka, Chem. Rev. 117 (2017) 11302–11336.
- [40] Y. Zhang, W.Q. Cui, W.J. An, L. Liu, Y.H. Liang, Y.F. Zhu, Appl. Catal. B: Environ. 221 (2018) 36–46.
- [41] C.C. Dong, Z.Y. Ma, R.T. Qie, X.H. Guo, C.H. Li, R.J. Wang, Y.L. Shi, B. Dai, X. Jia, Appl. Catal. B: Environ. 217 (2017) 629–636.
- [42] W.Y. Hu, W. Zhou, K.F. Zhang, X.C. Zhang, L. Wang, B.J. Jiang, G.H. Tian, D.Y. Zhao, H.G. Fu, J. Mater. Chem. A Mater. Energy Sustain. 4 (2016) 7495–7502.
- [43] S. Gao, Z.T. Sun, W. Liu, X.C. Jiao, X.L. Zu, Q.T. Hu, Y.F. Sun, T. Yao, W.H. Zhang, S.Q. Wei, Y. Xie, Nat. Commun. 8 (2017) 14503.
- [44] G.S. Li, Z.C. Lian, X. Li, Y.Y. Xu, W.C. Wang, D.Q. Zhang, F.H. Tian, H.X. Li, J. Mater. Chem. A Mater. Energy Sustain. 3 (2015) 3748–3756.
- [45] P.F. Xia, B.C. Zhu, J.G. Yu, S.W. Cao, M. Jaroniec, J. Mater. Chem. A Mater. Energy Sustain. 5 (2017) 3230–3238.
- [46] R.R. Hao, G.H. Wang, H. Tang, L.L. Sun, C. Xu, D.Y. Han, Appl. Catal. B: Environ. 187 (2016) 47–58.
- [47] S.L. Chen, D. Li, Y.X. Liu, W.X. Huang, J. Catal. 341 (2016) 126–135.
- [48] J. Liu, Y. Liu, N.Y. Liu, Y.Z. Han, X. Zhang, H. Huang, Y. Lifshitz, S.T. Lee, J. Zhong, Z.H. Kang, Science 347 (2015) 970–973.